

Collapse Analysis, Defect Sensitivity and Load Paths in Stiffened Shell Composite Structures

D.W. Kelly¹, M.C.W. Lee¹, A.C. Orifici^{2,3}
R.S. Thomson³ and R. Degenhardt^{4,5}

Abstract: An experimental program for collapse of curved stiffened composite shell structures encountered a wide range of initial and deep buckling mode shapes. This paper presents work to determine the significance of the buckling deformations for determining the final collapse loads and to understand the source of the variation. A finite element analysis is applied to predict growth of damage that causes the disbonding of stiffeners and defines a load displacement curve to final collapse. The variability in material properties and geometry is then investigated to identify a range of buckling modes and development of deep postbuckling deformation encountered in the experimental program. Finally the load paths for the damaged panels are used to visualise the load transfer and enhance the physical understanding of the load displacement history.

Keywords: Buckling, Stiffened Shells, Collapse Loads, Geometry Sensitivity.

1 Introduction

Composite skin-stiffened structures can withstand significant loads after initial buckling has occurred. However the application of composite postbuckling structures in curved aircraft panels has been limited to date due to concerns related to the sensitivity of the structures to manufacturing defects and service-induced damage. Unlike stiffened metallic fuselage panels, panels made from composite materials are not allowed to have degradation below the ultimate load due to issues relating to certification. In addition the analysis of these panels to model the progression of failure to collapse is non-trivial even using modern finite element (FE) solvers.

¹ University of New South Wales, Sydney, NSW, Australia

² Royal Melbourne Institute of Technology, Melbourne, VIC, Australia

³ Cooperative Research Centre for Advanced Composite Structures, Melbourne, VIC, Australia

⁴ German Aerospace Center, Braunschweig, Germany

⁵ Private University of Applied Sciences Göttingen, Stade, Germany

For undamaged skin-stiffened structures in compression, collapse is typically an explosive event caused by the initiation of separation between the skin and stiffeners followed by fibre failure and delamination. For pre-damaged structures, such as those taken from service or those used for damage tolerance and certification studies, the pre-damaged areas can grow under compression and contribute to the collapse if they are located at critical locations.

The European Commission 6th Framework project COCOMAT (Improved Material exploitation at Safe Design of Composite Airframe Structures by Accurate Simulation of Collapse) was a four year project aimed at exploiting the large reserve of strength in composite structures through more accurate prediction of collapse [Degenhardt, Rolfes, Zimmerman and Rohwer (2006); COCOMAT Home Page (2009)]. The Cooperative Research Centre for Advanced Composite Structures (CRC-ACS) was one of the 15 international partners involved in this project headed by the German Aerospace Center (DLR).

A range of thin stiffened shell panels were manufactured and tested in the COCOMAT project. When the results of the tests were reviewed it was found that a number of different buckling shapes were encountered in the experiments. In some cases it was not possible to match the shapes in FE analyses. For example, the panel shown in Figure 1 was tested in compression, and the experimental and numerical buckling patterns are shown in Figure 2 [Orifici, Thomson, Herszberg, Weller, Degenhardt and Bayandor (2008)]. The experiment showed an asymmetric postbuckling mode shape, which differed from the FE predictions of a symmetrical mode. The colour contours indicate normal displacement. The last image for the experimental result shows the vertical edges undergoing opposite displacements, while the FE results all show displacements of the same sign.

It was initially thought that the asymmetric postbuckling mode shapes encountered during physical testing were possibly due to three reasons, which were:

- (i) warping of the panels at curing and manufacture,
- (ii) imperfections in the stiffener blade width and
- (iii) asymmetric introduction of the load onto the panel.

The benchmark FE models did not include these variations and so it was not possible match to all the postbuckling mode shapes encountered in the experimental results.

Curved panels such as those modelled numerically and tested physically in COCOMAT are imperfection-sensitive and can exhibit different buckling mode shapes for small changes in the geometry and material data. This difference in postbuckling

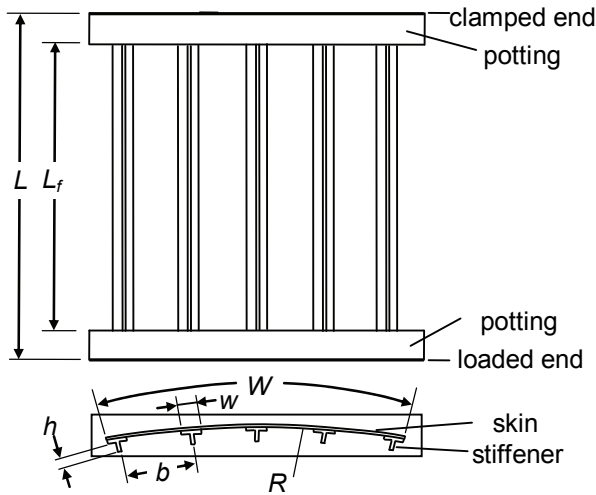


Figure 1: Geometrical representation of D1 panel

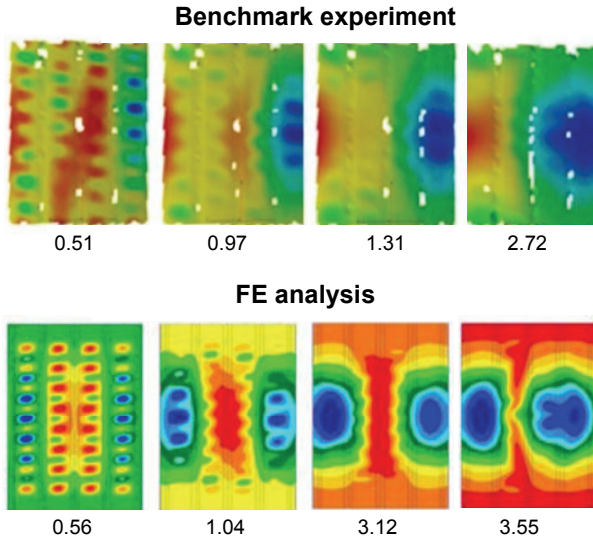


Figure 2: Benchmark experiment and FE analysis, buckling mode shape at applied axial compression (mm). FE analysis using MSC.Nastran (Nastran) [MSC.Software Corporation]

mode shapes directly affects the loading capability of the stiffened panel, and the manner in which the stiffeners fail in global buckling. Therefore particular attention was directed to determining the defects that occurred in the manufactured panels. Then the FE analyses in Orifici, Thomson, Degenhardt and Bayandor (2008) and summarised in this paper included modelling of the geometry of measured imperfections in order to match the experiments.

Attempts have been made in the recent years to introduce imperfections via stochastic modelling so as to achieve plausible knock down factors [Chryssanthopoulos and Poggi (1995); Raj, Iyengar and Yadav (1998); Spagnoli, Elghazouli and Chryssanthopoulos (2001)]. An investigation was conducted to determine the range of mode shapes due to imperfections in loading and boundary conditions for the COCOMAT panels [Lee, Kelly, Orifici and Thomson (2007); Lee, Thomson, Degenhardt and Kelly (2008)]. The range of the input values that were used was arbitrary but the results led to an investigation of the actual imperfection and variability resulting from manufacture. In the current pool of experiments it has been possible to collect data regarding the variation in material properties and geometry. It has also been possible to confirm by analysis that the scatter in mode shapes could be caused by the manufacturing defects and material variations. The defects and variations are also strong enough to affect the possible failure loads using FE analysis. A stochastic approach was therefore developed to introduce variability and it has been successfully applied to explain results that had previously been regarded as outliers in the experimental program.

The finite element analyses by CRC-ACS of the panels tested in the COCOMAT project have successfully captured the load-displacement history for a number of the panels tested [Orifici, Thomson, Herszberg, Weller, Degenhardt and Bayandor (2008)]. Only one panel will be considered in this paper. The geometry of this panel will be described in Section 2, together with the information gathered about the variation in material properties and geometry. The numerical algorithms that predict the initiation and growth of interlaminar damage and predict fibre failure leading to ultimate collapse are described in Section 3. The numerical algorithms enable the capture of the displacement behaviour and the analysis provides detailed information of the development and interaction of the various damage mechanisms. Section 4 describes the approach taken for the stochastic work [Lee, Payne, Kelly and Thomson (2008)]. Section 5 addresses the effect the variation could have on the geometry of the cured panels and Section 6 then searches for the buckling modes that were encountered in the experimental work. The research program also attempted to enhance the understanding of the physical response of the panels by improving the post-processing tools available in FE analysis. In modern FE packages the load field is not plotted and the distribution of the load in the pre-and

postbuckled structures is not clearly exposed. An attempt is therefore made in Section 6 to enhance the interpretation of the failure mechanisms by plotting load paths based on the theory presented in Kelly, Hsu and Asadullah (2001) prior and leading up to collapse.

2 DLR/CRC-ACS Design 1 (D1) Panel

Geometrical and material properties for the Design 1 (D1) panel are provided in this section. The D1 panel was designed by DLR and CRC-ACS. It was designed to have a large postbuckling region so that degradation in the skin-stringer bond could be observed. Geometrical representations for the panels can be found in Figure 1 and the geometrical properties can be found in Table 1. The panel consisted of a skin and blade-shaped stiffeners, with half the stiffener lay-up on each side used to form flanges and the skin and stiffeners separately cured then bonded with adhesive. Manufacturing the flanges in this manner meant that the 45 degree flange plies had reflective symmetry about the stiffener blade. A potting consisting of epoxy resin reinforced with sand and quartz was used at the ends of the panel to ensure an even application of the end load and prevent lateral movement in the testing machine.

The data presented in Table 2 are results obtained from the material characterisation of Hexcel IM7/8552 unidirectional carbon fibre epoxy used in COCOMAT [Lee, Thomson, Degenhardt and Kelly (2008)].

Table 1: Nominal panel geometry

Panel length, L (mm)	760
Panel free length, L_f (mm)	660
Panel Radius, R (mm)	1,000
Stiffener pitch, b (mm)	128
Number of stringers	5
Panel arc length, W (mm)	560
Stringer width, w (mm)	32
Stringer height, h (mm)	14.0
Skin-stringer joint	Bonded
Adhesive	FM 300
Skin lay-up	$[90, \pm 45, 0]_S$
Stiffener web lay-up	$[(45, -45)_3, 0_6]_S$
Stiffener flange lay-up	$[0_6, (45, -45)_3]$
Ply thickness (mm)	0.125
Material	Hexcel IM7/8552

Table 2: Nominal material properties for Hexcel IM7/8552

	Characterisation	
	Mean	Standard deviation
Stiffness		
E_{tL} (GPa)	164.1	5.1
E_{cL} (GPa)	142.5	2.4
E_{tT} (GPa)	8.7	0.3
E_{cT} (GPa)	9.7	0.5
G_{LT} (GPa)	5.1	0.7
Poisson's ratio		
ν_{LT}	0.277	0.04
Strength		
R_{tL} (MPa)	1741	207
R_{cL} (MPa)	854	77
R_{tT} (MPa)	28.8	5.2
R_{cT} (MPa)	282	14.4
R_{LT} (MPa)	98.2	17.2

2.1 Variations in geometry of the stiffened panel

One of the obvious disparities between the manufactured panel and the panels analysed using FE is the difference in the initial geometry. The panels which are manufactured have been subjected to residual stresses caused by the curing process while those in the FE environment are perfect, with the exception of minor geometrical variation caused by numerical rounding in the pre-processor. The curing process has resulted in the panels taking on varying nominal radii of curvature, thereby affecting the buckling behaviour and final collapse load. This variation in radius has been noted in Table 3, which shows the mean, standard deviation (STDEV) and range of values measured on several experimental panels. The measurement of geometrical imperfections and actual radius was performed at the DLR using the 3D optical measurement system ATOS [GOM GmbH (2009)].

3 FE Analysis to Predict Collapse

An analysis methodology has been developed at CRC-ACS to predict the collapse of stiffened composite structures in compression that is focused on capturing the effects of the critical damage mechanisms. The approach contains several aspects: predicting the initiation of interlaminar damage in intact structures; capturing in-plane degradation such as fibre fracture and matrix cracking; and capturing the

Table 3: Measured panel geometry values (mm)

	Mean	STDEV	Range		
L_f	658.63	0.067	657.5	–	659
R	937.25	11.87	864	–	1034
b	132.65	0.49	132	–	133
W	560.4	0.24	558	–	561
w	32.37	1.40	31.5	–	33.0
h	14.36	0.82	14.1	–	14.5

propagation of a pre-existing interlaminar damage region [Orifici (2007); Orifici, Thomson, Degenhardt, Bisagni and Bayandor (2009a,b)].

The complete analysis methodology, combining the global-local analysis for interlaminar damage prediction and degradation models for interlaminar damage growth and in-plane damage, was implemented into Marc v2005r3 (Marc) [MSC.Software Corporation] by a combination of user subroutines. The methodology allows for a complete analysis of the postbuckling and collapse behaviour of composite structure designs, including the effects of damage. The features of the methodology make it suitable in both a design and comparative analysis context for application to both intact and pre-damaged structures.

3.1 Interlaminar damage initiation

The approach for predicting the initiation of interlaminar damage in the skin-stiffener interface was based on a two-step global-local technique illustrated in Figure 3. In this approach, a coarse model of the entire structure was constructed using computationally efficient shell elements, and combined with local models of the skin-stiffener interface cross-section that used three-dimensional (3D) solid brick elements. The global shell model was used to determine the deformation field of the entire structure, which was then input as boundary conditions on a local 3D model of a skin-stiffener interface.

A strength criterion monitored all elements in the local model in order to predict the initiation of delamination or skin-stiffener separation. The criterion applied was the “degenerated Tsai” equation as given by Tong (1997) and was defined as

$$(\sigma_x/X_T)^2 + (\sigma_z/Z_T)^2 + (\tau_{yz}/S_{yz})^2 \geq 1, \quad (1)$$

where σ_x , σ_z , τ_{yz} and X_T , Z_T , S_{yz} are stresses and strengths in the local longitudinal, through-thickness tensile and shear directions, respectively. The longitudinal stress is included in this equation as it was found to influence delamination initiation in

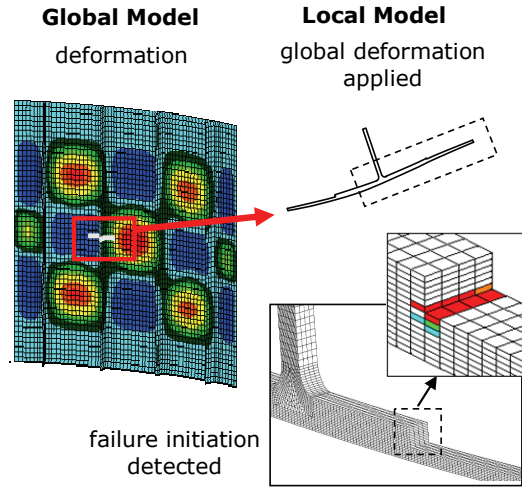


Figure 3: Global-local approach for detecting initiation of skin-stiffener delamination [Orifici, Thomson, Degenhardt, Bisagni and Bayandor (2009a)]

composite joints, particularly for plies adjacent to an adhesive layer [Tong (1997)]. Failure was deemed to occur when the average of all integration point values in an element satisfied this criterion. By modifying the location of the 3D local model, the initiation of interlaminar damage throughout the panel could be investigated in order to determine the most critical skin-stiffener interface location. Failure prediction in this manner is sensitive to the element length at the flange edge, which in this work was taken from previous calibration studies on skin-stiffener sections [Orifici, Thomson, Herszberg, Weller, Degenhardt and Bayandor (2008)].

3.2 Ply damage model

For the ply damage degradation model, an approach was developed for capturing in-plane damage occurring within the plies of the composite material. The Hashin (1980) failure criteria and stiffness reduction method of Chang and Lessard (1991) were used to define ply damage and failure. These criteria are summarised in Table 4, where σ_{11} , σ_{22} , τ_{12} and X , Y , S_{12} are stresses and strengths in the fibre, in-plane transverse and shear directions, S_{23} is the through-thickness shear strength (assumed equal to S_{12} for a transversely isotropic ply), and subscripts T and C refer to tension and compression. The criteria for fibre failure, matrix cracking and fibre-matrix shear failure were monitored and used to reduce selected material properties to zero upon detection of failure, where all properties were reduced for fibre failure, E_{22} was reduced for matrix failure, and G_{12} and G_{31} were reduced for shear failure.

Table 4: In-plane failure criteria

Failure type	Criterion
Fibre, tension	$(\sigma_{11}^2/X_T^2)^{\frac{1}{2}} \geq 1$
Fibre, compression	$(\sigma_{11}^2/X_C^2)^{\frac{1}{2}} \geq 1$
Matrix, tension	$(\sigma_{22}^2/Y_T^2 + \tau_{12}^2/S_{12}^2)^{\frac{1}{2}} \geq 1$
Matrix, compression	$\left(\frac{\sigma_{22}}{Y_C} \left(\frac{Y_C^2}{4S_{23}^2} - 1\right) + \frac{\sigma_{22}^2}{4S_{23}^2} + \frac{\sigma_{12}^2}{4S_{12}^2}\right)^{\frac{1}{2}} \geq 1$
Fibre-matrix shear, tension	$(\sigma_{12}^2/S_{12}^2)^{\frac{1}{2}} \geq 1$
Fibre-matrix shear, compression	$(\sigma_{11}^2/X_C^2 + \sigma_{12}^2/S_{12}^2)^{\frac{1}{2}} \geq 1$

3.3 Interlaminar damage growth

In the interlaminar damage growth model [Orifici, Thomson, Degenhardt, Bisagni and Bayandor (2007)], pre-existing interlaminar damage in the skin-stiffener interface was represented as a debonded region between the skin and stiffener. Shell layers were connected with user-defined multi-point constraints (MPCs). The user-defined MPCs were given one of three “states”, which were used to define the intact (state 0), crack front (state 1) and debonded (state 2) regions as shown in Figure 4. Gap elements were used in any debonded region to prevent crossover of the two sublaminates. To model the correct bending behaviour the shell layers were separated by a nominal distance (0.002 mm) so as to be coincident, and the respective laminates offset using dummy plies.

At the end of every nonlinear analysis increment, the Virtual Crack Closure Technique (VCCT) [Rybicki and Kanninen (1977)] was used to determine the strain energy release rates at all MPCs on the crack front. The VCCT equations accounted for arbitrary element sizes, and an algorithm was written to determine the local crack front coordinate system from the neighbouring crack front nodes, following recommendations given by Krueger (2004). The onset of propagation was determined using the B-K criterion [Benzeggagh and Kenane (1996)], with modification for the inclusion of the mode III component following the suggestion given by Camanho and Dávila (2003), given by

$$\frac{G_I + G_{II} + G_{III}}{G_{IC} + (G_{IIC} - G_{IC}) \left(\frac{G_{II} + G_{III}}{G_I + G_{II} + G_{III}}\right)^\eta} = 1, \quad (2)$$

where G are the strain energy release rates in modes I, II and III, G_C are fracture toughness values, and η is a curve fit parameter found from mixed-mode test data. For crack propagation, an iterative method was applied that reduced the strain en-

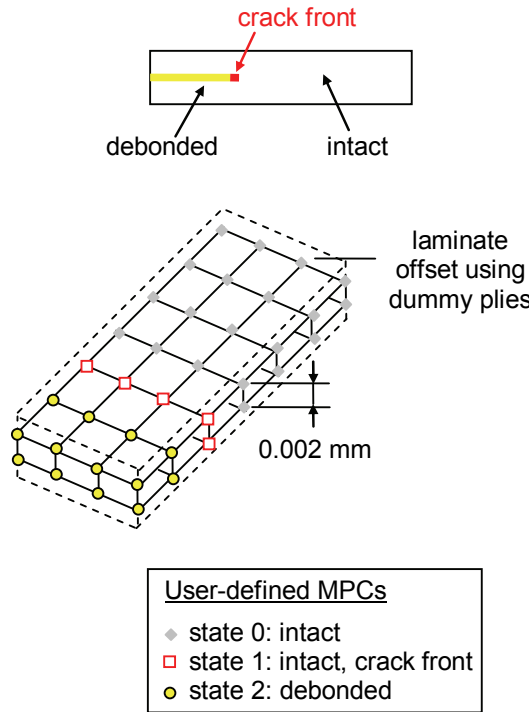


Figure 4: Interlaminar damage modelling with user-defined MPCs [Orifici, Thomson, Degenhardt, Bisagni and Bayandor (2009a)]

ergy release rate values based on the shape of the local crack front at each MPC. This was developed as it was found that the local crack front affected the estimation of crack opening displacement, which in VCCT is based on self-similar crack growth. Modification factors were determined to account for the difference in crack opening between the actual crack propagation and the assumed self-similar case. Further information on this approach has been presented in previous publications [Orifici, Thomson, Degenhardt, Bisagni and Bayandor (2009a); Orifici, Thomson, Degenhardt, Bisagni and Bayandor (2007)]. In the analysis applied in this work, the interlaminar damage is modelled at the skin-stiffener interface.

3.4 Experimental and numerical results

In this section, results are presented for the multi-stiffener curved panel in Figure 1 and Table 1. The panel was manufactured by Aernnova Engineering Solutions and tested by the Institute of Composite Structures and Adaptive Systems of DLR

as part of the COCOMAT project. Following manufacture, panel quality was inspected with ultrasonic and thermographic scanning. The manufactured geometry of the panel was measured using ATOS. During the test, measurements were taken using displacement transducers (LVDTs), strain gauges, the 3D optical measuring system ARAMIS [GOM GmbH (2009)], and optical lock-in thermography. Further detail on all the inspection and data measurement systems can be found in Degenhardt, Kling, Klein, Hillger, Goetting, Zimmermann, Rohwer and Gleiter (2007). Testing of the panel involved static loading in compression until collapse.

No damage was detected from the ultrasonic and thermographic scanning that followed manufacture. In testing, the panel was loaded with 2000 cycles up to 1.08 mm compression, 1700 cycles up to 1.93 mm compression, then statically until collapse. The cyclic loading corresponded to loads just before global buckling, and 95% of the expected displacement at collapse. Following an assessment of the results, it was seen that the cyclic loading, particularly the 95% loading, caused damage to occur in the panel that was considered as pre-damage for the final static loading to collapse. This pre-damage is shown in Figure 5, and was detected using thermographic scanning. The pre-damage corresponded to a debonded area of 2016 mm² under the centre stiffener and 1920 mm² under the inner stiffener.

In the numerical analysis, an FE model was created based on the analysis methodol-

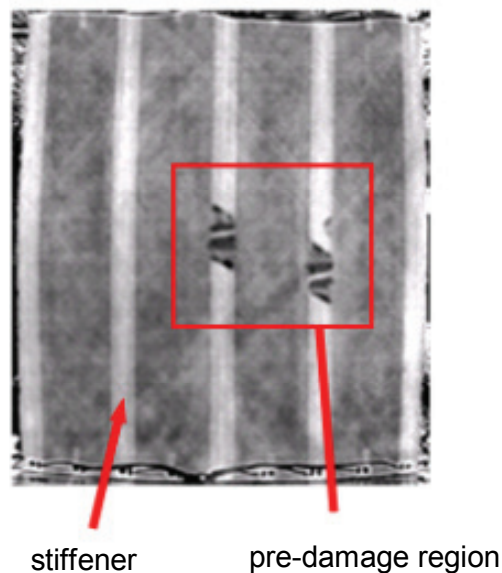


Figure 5: Skin-stiffener pre-damage after 3700 cycles

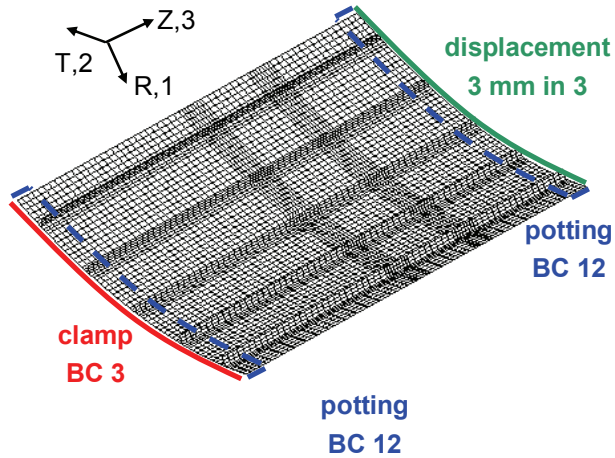


Figure 6: FE model with boundary conditions (BC) [Orifici, Thomson, Degenhardt, Bisagni and Bayandor (2009a)]

ogy described, and consisted of 6,004 nodes and 5,772 shell elements. The boundary conditions and FE mesh are shown in Figure 6. Fracture properties for the model are given in Table 5. User-defined MPCs were included between the skin and stiffener of the centre and an inner stiffener, in order to model the debond growth seen in the experiment. Skin-stiffener debonds were created as pre-damage by setting the MPCs to the appropriate states. The pre-damaged debonded regions were taken from the thermographic scans of the damage, and were adapted to the regular grid mesh of the model to match the area and shape of the experimental damage sites. It was assumed that the cyclic loading only resulted in skin-stiffener debonding, and any other damage such as matrix cracking that could have been present in the panel prior to static loading was not considered.

Comparison between the experimental and numerical results is given below, where

Table 5: Fracture properties for IM7/8552 carbon/epoxy unidirectional tape

Fracture property	Value
G_{Ic} [kJ/m ²]	0.243
G_{IIc} [kJ/m ²]	0.514
G_{IIIc}^* [kJ/m ²]	0.514
B-K coefficient, η^*	4.6

* assumed

Figure 7 is the load response, Figure 8 gives the out-of-plane displacement and Figure 9 illustrates the debond growth following collapse.

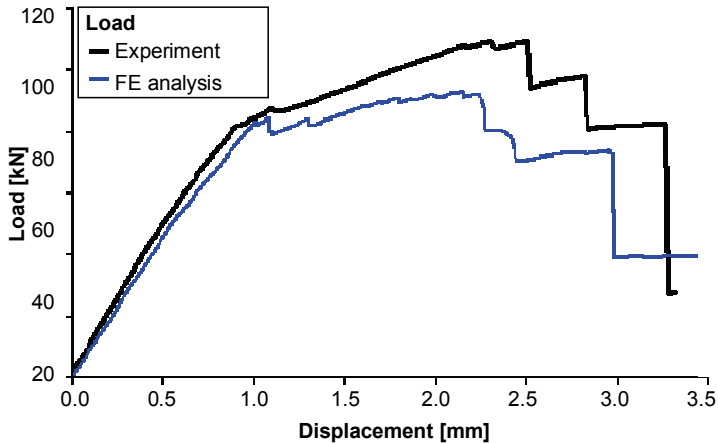


Figure 7: Experimental and numerical load-displacement results

Under loading the experimental panel developed a range of buckling patterns as shown in Figure 8. A local buckling pattern of 13 to 15 longitudinal half waves per stiffener bay developed at around 0.75 mm axial compression, leading to global buckling at around 1.0 mm axial compression. The global buckling pattern was symmetric and consisted of an inwards buckle (towards the stiffener side) located over the centre stiffener and outwards buckles in the outer stiffener bays. Under further compression the central buckle moved to one of the inner stiffener bays creating an asymmetric pattern.

Opening of the debonded regions was evident by 2.5 mm axial compression. At around 2.5 mm axial compression the debonded areas showed a rapidly increased damage growth and opening displacement, which caused a large reduction in the load-carrying capacity of the panel as shown in Figure 7. The damage growth process was seen again at around 2.81 mm axial compression, where growth of the debonded area led to an increase in the skin-stiffener opening, and also caused some fibre fracture and matrix cracking in the regions around the debonds. Collapse of the panel occurred at 3.31 mm axial compression and corresponded to significant fibre fracture through the centre stiffener.

The numerical analysis was performed using the nonlinear solver in Marc, with a full Newton-Raphson procedure and a load residuals tolerance of 0.01. From Figure 8, the FE model gave a local buckling pattern of 15 half waves per bay and

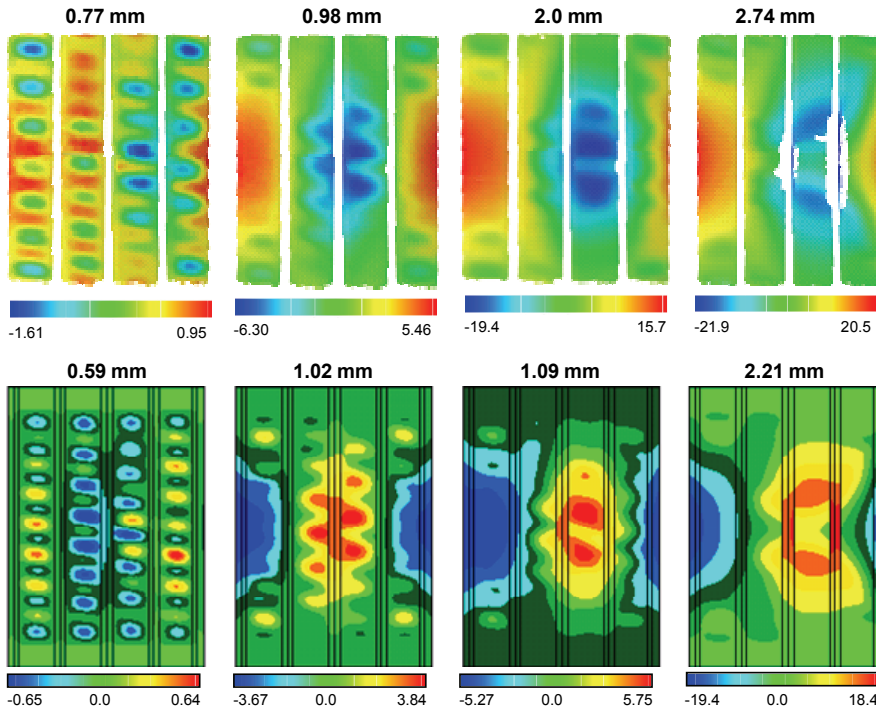


Figure 8: Experimental (top) and numerical (bottom) out-of-plane displacement (mm) at applied axial compression. For the numerical results positive displacement is towards the centre of curvature of the panel

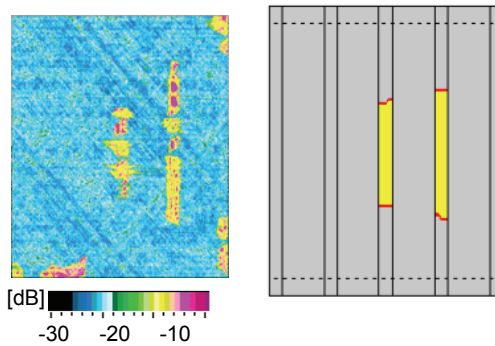


Figure 9: Collapsed panel. Left: Ultrasonic scan of experimental panel. Right: FE model skin-stiffener debonds

global buckling of a single central buckle at 1.02 mm compression that moved to be located between two inner stiffeners by 1.09 mm compression. This behaviour agreed very well with the experimental behaviour. The buckling behaviour can also be observed in Figure 7 from drops in the load curve and changes in the panel stiffness. In the numerical model, the movement of the global buckle coincided with coalescence of the separate debonded regions under the two stiffeners, and some opening was seen across these interfaces. Growth of the debonded regions was then predicted to occur in a continuous manner, and was characterised by drops in the load response and increased skin-stiffener opening. Crack growth was accompanied by matrix cracking in mainly the outer 90° plies of the skin, which was focused on the centre and edges of the debonded regions. Though correspondence was not seen at all predicted locations, the experimental panel did show matrix cracking in outer plies extending from the skin-stiffener debond edges.

Under further compression, the numerical model showed fibre fracture in mainly the central 0° stiffener plies at 2.25 mm, 2.35 mm and 2.96 mm axial compression, with the two outer stiffeners and an inner stiffener failing sequentially. Fibre fracture was characterised by large drops in the load response of the panel of around 10 kN for the outer stiffener failures, and around 30 kN for the inner stiffener, where the latter was taken as the collapse of the panel. Though the experimental panel showed failure in the central stiffener causing collapse, the sequence and size of the load reductions, the onset of fibre fracture in the central 0° plies of the stiffeners, and the way in which the debond growth and matrix cracking contributed to fibre fracture and panel collapse all closely matched the experimental results.

Whilst it was difficult to extract precise crack growth data from the experimental results, crack opening was seen at several stages before and after fibre fracture, and the experimental debonded area under the inner stiffener showed greater crack growth. Both of these aspects were seen in the numerical model, and in general the crack growth behaviour compared well with the experimental results. The numerical model predicted crack growth to occur just after buckling, which was earlier than seen in the experimental panel. This led to the underestimation of the panel load, particularly at higher values of axial compression. Additionally, as shown in Figure 9 the approximate final debonded lengths of the experimental panel were 224 mm and 403 mm under the central and inner stiffener respectively, which gave very good comparison with the numerical values of 282 mm and 316 mm, especially considering the fact that fibre fracture in the experimental panel would have caused additional crack growth and energy release.

4 Stochastic Methodology

A stochastic analysis methodology was developed in which a family of m panels is analysed with each of the input variables varied in a random fashion. The methodology is therefore multi-variant, and consists of a sample size of m configurations with n input variables that take a random value within a range. The m output responses are obtained through repeated analyses.

The results of the analyses are used to generate n metamodells for each output response. The i^{th} metamodel for a selected output response measures the output against the value of the i^{th} input variable for all members of the family of panels. There are therefore m points on the plot.

Once the metamodells are generated, *influence* and *sensitivity* can be derived. A Spearman Correlation is performed in order to find the influence of each input variable on the output response. The Spearman Correlation is a nonlinear correlation that can be used at the ordinal level. The formulation for the Spearman Correlation, ρ , is:

$$\rho = \frac{\sum_{i=1}^m R(X_i)R(Y_i) - m \left(\frac{m+1}{2}\right)^2}{\sqrt{\sum_{i=1}^m R(X_i)^2 - m \left(\frac{m+1}{2}\right)^2} \sqrt{\sum_{i=1}^m R(Y_i)^2 - m \left(\frac{m+1}{2}\right)^2}} \quad (3)$$

where R is the ordinal rank, Y_i is the output response, X_i is the input variable and m is the number of samples in the metamodel.

An influence factor of unity can be interpreted as an output being proportional to the input variable. Conversely if the influence factor is -1, it can be concluded that the output response is inversely proportional to the input variable. The next step is to find the sensitivity of output to the input variable. Sensitivity β can be found using the least-squares method. The formulation is given below, where the bar indicates the mean value.

$$\beta = \frac{\sum_{i=1}^m (X_i - \bar{X})(Y_i - \bar{Y})}{\sum_{i=1}^m (X_i - \bar{X})^2} \quad (4)$$

It is a requirement that the sensitivities with respect to the input variables are first scaled so that any skew effects in the final result due to the scale of each input can be removed. The scaling problem is frequently encountered when analysing composite structures where, for example, the longitudinal Young's modulus is a factor of 10^5 while Poisson's ratio exists at a factor of 10^{-1} . In order to scale the sensitivity with respect to the output variable, it has to be considered with the nominal mean μ_X of the input variable X . Scaled sensitivity B_X can be obtained as follows:

$$B_X = \beta_X \mu_X, \quad (5)$$

With influence and scaled sensitivity it is possible to derive a Robust Index (RI) with respect to the input variable that is useful in design. The index is also useful in assessing whether a particular panel will be sensitive to variations in the material properties and geometry in an experimental investigation. It is evaluated for each output response and for each variable, using the expression

$$RI_i = \frac{1}{\rho_{X_i} B_{X_i}}. \quad (6)$$

Clearly a design is robust with respect to changes in a design variable if the sensitivity is small. However, the product ρB is used here because each sample point in the metamodel shows the effect of simultaneous variation of all the variables. A low correlation between the output and input variable in the metamodel indicates other variables are causing the change and so the effect of a higher sensitivity can be reduced. The measure of robustness for the design is then the absolute of the minimum recorded for the indices across all variables and all output responses.

In the stochastic analysis the material, laminate and boundary conditions are varied to show their impact on panel behaviour. Using the stochastic methodology it is possible to reveal *a priori* the possible postbuckling response of the panel before experiments are conducted.

5 Stochastic Analysis of the Curing Process

One difference between the manufactured panel and the FE models is the initial geometry. Manufactured panels contain deformation and residual stresses caused by the curing process, while the FE models are perfect except for minor geometrical variation caused by numerical rounding in the pre-processor. The curing process results in the panels taking on varying nominal radii of curvature, which then significantly affects the buckling behaviour and final collapse load. The effect of variation in material properties on the curing process was investigated using the stochastic analysis approach described and the D1 panel.

Gaussian normal inputs were chosen for the input variables. The variations introduced in the material properties of the lamina were chosen based on data obtained during material characterisation. The lamina orientations contained a variation ranging up to 3.4 degrees about the mean value while the lamina thickness had a variation of 2.5%. Table 6 shows the deterministic input values and the corresponding stochastic variation used. The values in the defined range are from -3 to +3 standard deviations about the mean.

The panels were modelled using 5460 shell elements with the MSC.Patran pre-processor [MSC.Software Corporation]. The skins and stiffener flanges were modelled as single laminates and offsets were applied to model the skin-stiffener joint

Table 6: Stochastic boundary for analysis of D1 panel

	Mean	Range		
E_{11} (GPa)	142	135	–	150
E_{22} (GPa)	9.75	8.33	–	11.2
ν_{12}	0.277	0.237	–	0.317
G_{12} (GPa)	5.13	3.014	–	7.24
G_{23} (GPa)	4	3.4	–	4.6
G_{13} (GPa)	5.13	3.014	–	7.24
0° ply orientation (°)	0	-3.38	–	3.38
45° ply orientation (°)	45	41.6	–	48.4
-45° ply orientation (°)	-45	41.6	–	48.4
90° ply orientation (°)	90	41.6	–	48.4
Ply thickness (mm)	0.125	0.116	–	0.134

accurately. The panels were analysed using the Nastran nonlinear solver. The curing process was simulated using a change in model temperature from 177°C to room temperature, as per the Hexcel data sheet [Hexcel Corporation (2005)]. The longitudinal coefficient of thermal expansion (CTE) used was $-0.4 \times 10^{-6}/^{\circ}\text{C}$ and the transverse CTE was $5.6 \times 10^{-6}/^{\circ}\text{C}$ [Kulkarni and Ochoa (2006)]. In total 40 panels were analysed, each with stochastic variation of material properties. A sample of the results of the investigation is shown in Figure 10, where actual displacements from several manufactured panels are shown to be reasonably well predicted by the stochastic analysis approach. The measurements for the manufactured panels were done using the ATOS system.

Metamodels of the deformation are plotted against the stiffness of the first two skin plies in Figure 11. It was found that the stiffness of the first two skin plies was significant in affecting the curing deformation; the influence was 0.516 and 0.458 respectively. This high influence is due to the positioning of the plies furthest from the neutral axis. The stochastic analysis also indicated that the amount of deformation in curing was significantly larger once variation was incorporated. The nominal panel had a net deformation of 0.57 mm while the net mean deformation obtained from the stochastic analyses was 1.95 mm.

6 Stochastic Analysis of Postbuckling Performance

The stochastic analysis approach was used to investigate the postbuckling response of the D1 panel. As there was a possibility that uneven loading in the through-thickness direction of the panel could contribute to a variation in buckling re-

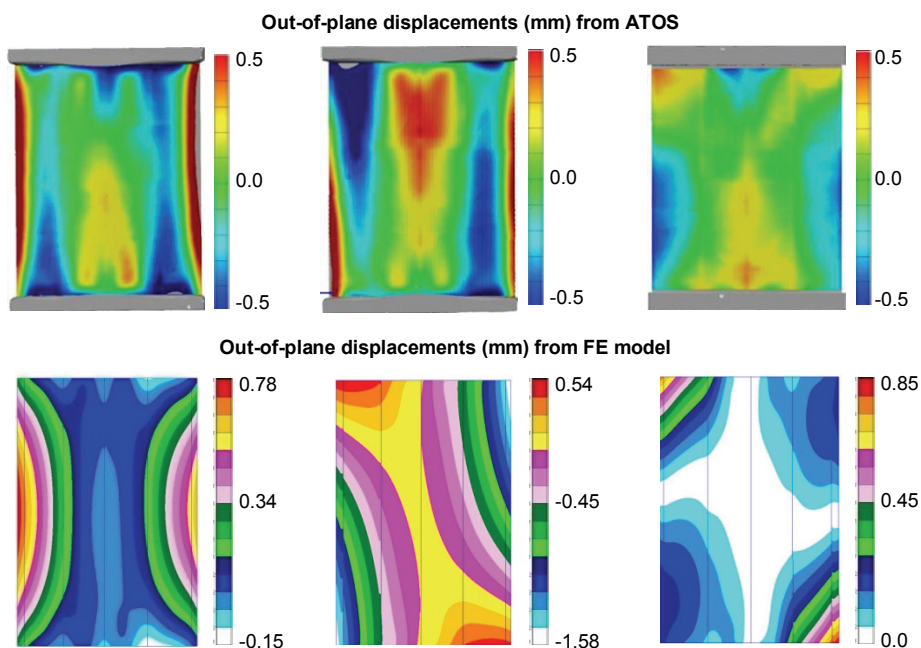


Figure 10: Panel geometric imperfections due to the curing process. Top: Experimental data measured using ATOS. Bottom: Selected FE results from stochastic analysis

sponses, this was included into the stochastic analysis. A node was created at the centre of curvature and connected with rigid links to all the nodes on the loaded edge, as shown in Figure 12. This was done so that a rotation θ_z could be added to the axial displacement loading, to simulate the effect of uneven loading.

A stochastic analysis was performed with a sample size of 40 panels, where the model properties were varied as shown in Table 6, and the angular rotation varied between -0.15° and 0.15° . The panels were analysed using the nonlinear solver in Marc, though no degradation models were applied as the focus of the investigation was the postbuckling performance and not the panel collapse.

The results of the stochastic analysis are presented in Table 7, where the input parameters and key terms of the blade and skin laminate stiffness matrix are quantified with respect to the panel maximum compressive load. The panel compressive load was taken at 2 mm axial compression, and was selected as the output variable as it is a key parameter for the postbuckling load-carrying capacity. This load is dependent on the postbuckling mode, which is another important factor considered in

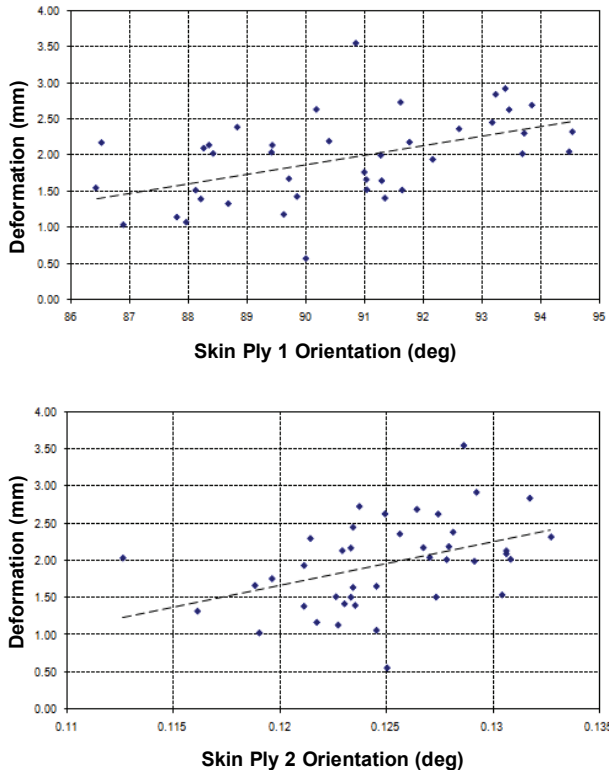


Figure 11: Metamodels of deformation against Ply 1 orientation (top) and Ply 2 thickness (bottom)

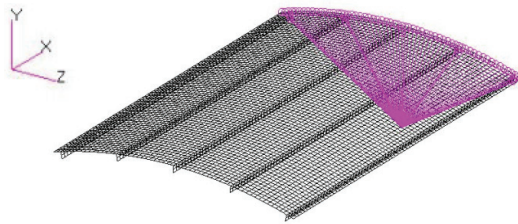


Figure 12: FE model with rigid links at the loaded end

processing the analysis results. From the results in Table 7, the fibre axis modulus E_{11} and the skin and blade laminate stiffness component A_{11} have the most effect on the load-carrying capability of the panels.

Figure 13 shows the metamodels of the key input variables affecting the failure

Table 7: Results from stochastic analysis of the D1 panel with respect to the panel load at 2 mm compression

		ρ	$\beta \times 10^{-4}$	B	RI
Material	E_{11}	0.337	6.25	89.3	0.0334
	E_{22}	0.250	1.80	17.5	0.229
	ν_{12}	-0.0921	-1.23	-3.42	3.18
	G_{12}	0.498	3.22	16.4	0.122
	G_{23}	0.0713	2.49	10.1	1.39
	G_{13}	0.498	3.22	16.4	0.122
Skin	A_{11}	0.314	5.63	34.1	0.0935
	B_{11}	-0.172	-2.25	0.194	-30.0
	D_{11}	0.0779	2.92	6.33	2.03
Blade	A_{11}	0.497	2.20	62.3	0.0323
	B_{11}	-0.110	-1.07	0.0245	-372
	D_{11}	0.434	2.9	37.9	0.0608
Rotation	θ_z	0.171	1.00	0.0251	234

load. These are the longitudinal Young's modulus and blade stiffness component A_{11} .

From the stochastic analysis, five samples representative of the results obtained are shown in Figure 14. As no degradation models have been applied, the drops and changes in the plots are due to postbuckling mode shape changes. From the plots it can be seen that the panels generally have a similar maximum loading capability but this level of loading occurs at various compressive axial displacements. The area under the load shortening curves represents the energy that each panel is able to withstand as a compressive displacement is applied. Failure is assumed to have occurred when there is a large drop in the load shortening curve. This drop is a function of the change in geometry as it snaps through the various postbuckling modes.

In Figure 15, the out-of-plane displacement plots corresponding to the load shortening curves in Figure 14 are shown. The plots show the panel from the stiffener side, where the regions in white are displacements towards the centre of curvature while the red regions are in the opposite direction. It can be seen that, in general, there are three different postbuckling mode shapes in the deep postbuckling regions as shown in the sixth plot for each sample. Also it can be observed that although Samples 2, 8 and 32 have asymmetric postbuckling mode shapes in the deep postbuckling regions at 2.72 mm, 2.24 mm and 2.62 mm compression respectively, the

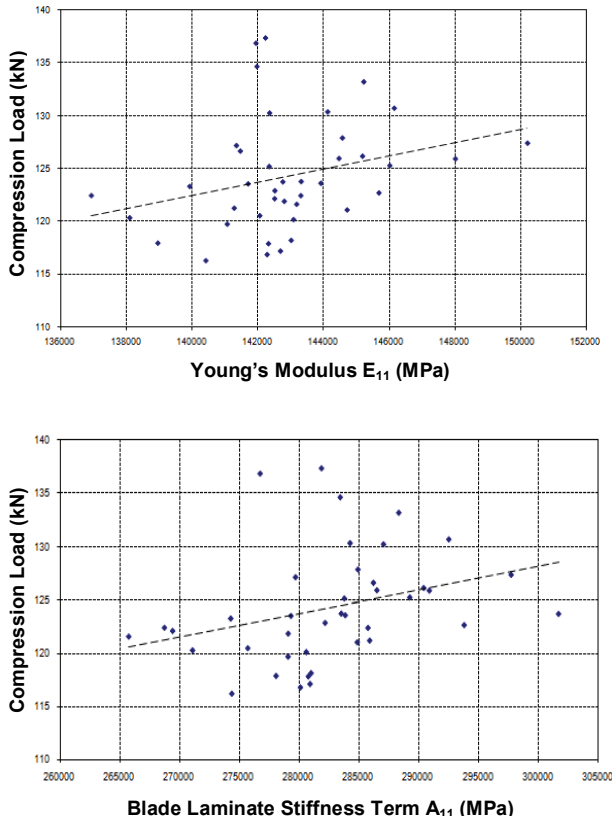


Figure 13: Metamodels for maximum compression load against Young's modulus (top) and stiffness component A_{11} of the blade laminate (bottom)

various buckling modes that the panels transition through are different.

Figure 16 presents two panels tested by the Institute of Composite Structures and Adaptive Systems of DLR as part of COCOMAT. These panels were known internally as P29 and P30, where results for the P29 panel were also presented in Section 3. Together with the benchmark experiment, these results are in good agreement with those obtained from the stochastic analysis. Good matches in buckling modes can be made between the benchmark panel in Figure 2 and Sample 32, P29 and Sample 20, P30 and Sample 9.

The introduction of imperfections and variations caused each laminate in the panel to no longer be symmetrical. Coupled with the introduction of nonlinear loading, it can be seen that the panel no longer experiences pure compression. Instead, there

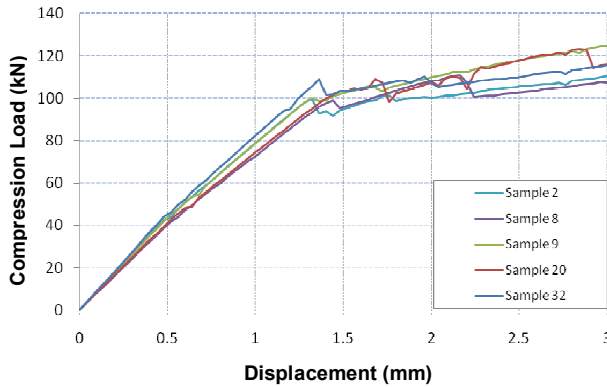


Figure 14: Sample load shortening curves obtained from stochastic analysis using FE

is a small bending component that also contributes to the variations in buckling modes seen in the stochastic analysis. Figure 17 is an extract of the results where the postbuckling mode shapes at 3 mm axial compression are plotted against the angular rotation that has been applied at the MPC. Each marker represents a FE result from the stochastic analysis. Note the bifurcation that exists in the results of the plot. Within the range of variations included in the plots, a panel with defects can undertake any of the three postbuckling mode shapes shown on the right of the plot. This reveals the level of instability that exists in the design and thus a lack of robustness.

7 Load Path Plots

As part of this investigation an attempt has been made to enhance the physical understanding of the behaviour of the panels and to investigate the type of defect and the location of defects that most influence the results. A statement often made is that defects on primary load paths are important but no FE system offers tools to identify these paths.

The theory for plotting load paths is described elsewhere [Kelly, Hsu and Asadullah (2001)], and is only summarised here. The components of stress at a point in a structure form a first order tensor and can be represented in a $[3 \times 3]$ matrix. If each row gives the three stresses acting on a plane whose normal is aligned with one of

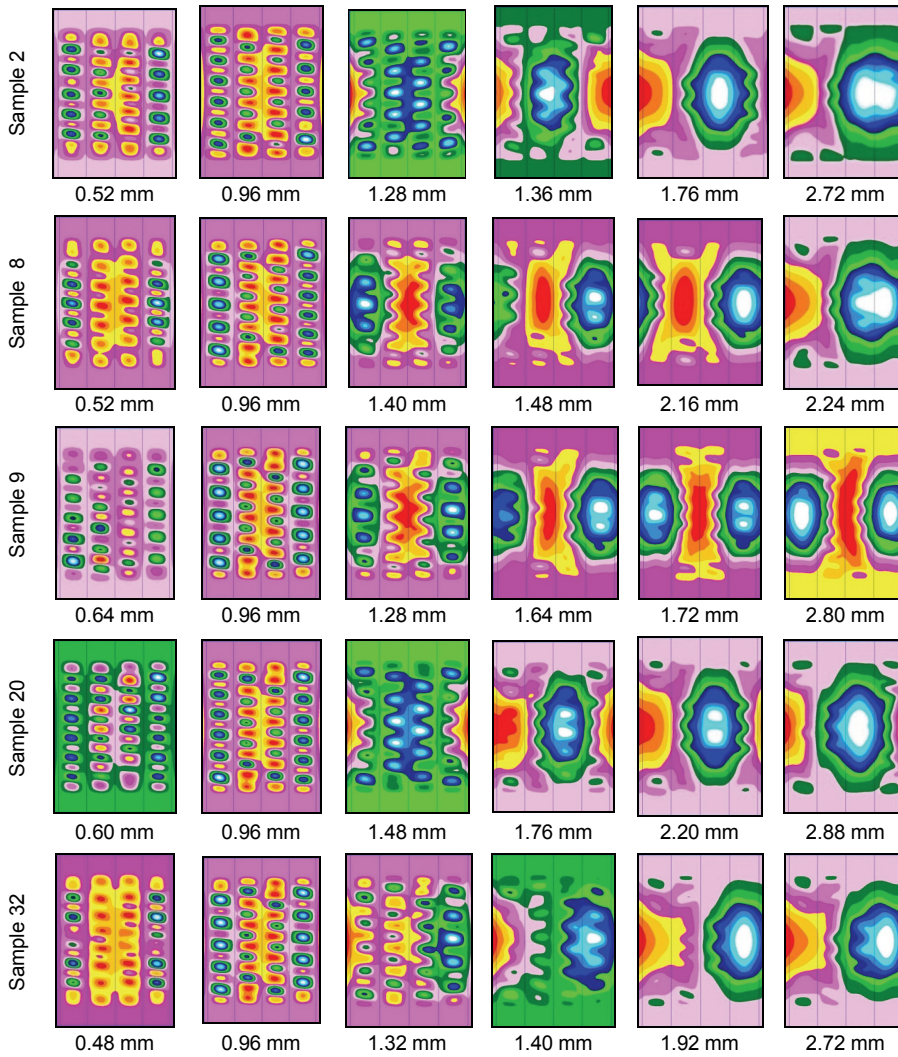


Figure 15: Out-of-plane displacement at axial compression (mm) for panels corresponding to the load shortening curves in Figure 14

the coordinate axes, then

$$[\sigma] = \begin{bmatrix} \sigma_{xx} & \tau_{xy} & \tau_{xz} \\ \tau_{yx} & \sigma_{yy} & \sigma_{yz} \\ \tau_{zx} & \tau_{zy} & \sigma_{zz} \end{bmatrix}. \quad (7)$$

Here τ_{xy} is the shear acting on the plane whose normal is in the x-direction, directed

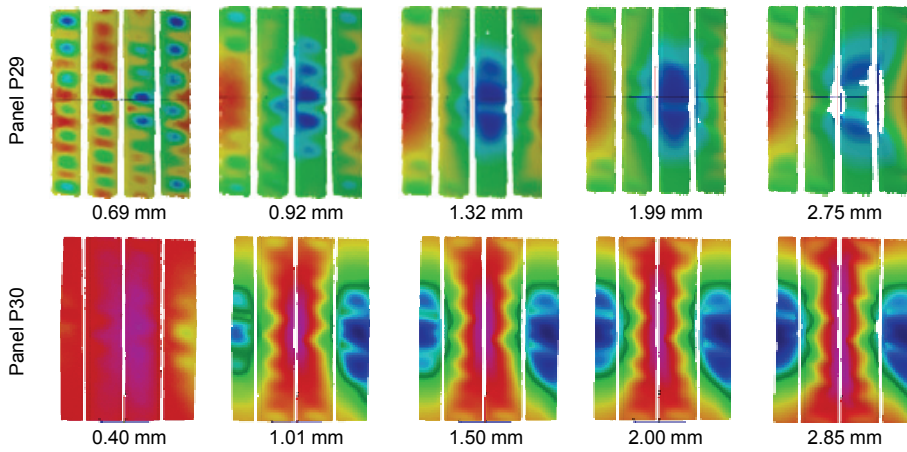


Figure 16: Out-of plane displacement at axial compression (mm) of two experimental D1 panels tested in COCOMAT

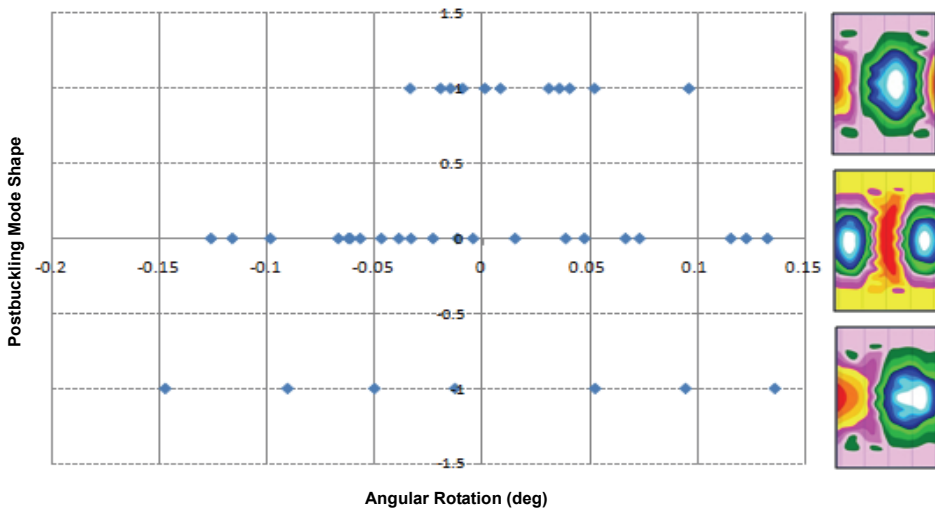


Figure 17: Plot of postbuckling mode shape at 3 mm compression against applied rotation from the stochastic FE analyses

positive in the positive y -direction. Eigenvalues and eigenvectors of this matrix provide the principal stresses and principal stress vectors.

Load paths can be defined by plotting contours aligned with total stress “pointing” vectors given by the columns of the stress matrix. Each column of the matrix gives the stress component in the corresponding coordinate direction on the three planes that form the sides of an elemental cube surrounding a point. The pointing vectors are thus defined at every point in the domain by

$$\begin{aligned} V_x &= \sigma_{xx}i + \tau_{yx}j + \tau_{zx}k \\ V_y &= \tau_{xy}i + \sigma_{yy}j + \tau_{zy}k \\ V_z &= \tau_{xz}i + \tau_{yz}j + \sigma_{zz}k \end{aligned} \quad (8)$$

where i , j and k are unit vectors in the x , y and z directions. The forces acting on an arbitrary plane in Figure 18a that sections the element with normal given by $\vec{n} = n_xi + n_yj + n_zk$ are obtained by integrating the total stress vectors, giving the equations below, where the dot indicates the dot product.

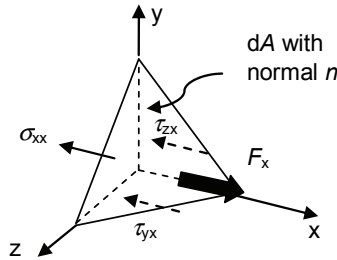
$$\begin{aligned} F_x &= \int V_x \cdot \vec{n} dA \\ F_y &= \int V_y \cdot \vec{n} dA \\ F_z &= \int V_z \cdot \vec{n} dA \end{aligned} \quad (9)$$

The load path for a force in a given direction is a region in which the force in that direction remains constant. For example, if the path in Figure 18b is to define a region in which the force P_x remains constant, the requirement is to determine the curved contour forming an edge along which the normal and tangential edge loads make no contribution to force in the x -direction. This requires that there is no contribution to the x -force on sides AB and CD. On AB this requires $F_x|_{AB} = 0$ or $\int_A^B V_x \cdot \vec{n} dA = 0$. This is achieved if the normal to the surface is perpendicular to V_x , as the dot product is then zero. Alternatively, this is achieved if the surface tangents are parallel to the vector V_x as indicated in Figure 18b.

Separate load path vectors are defined for load transfer in the x , y and z directions. Fortunately this does not restrict the paths to these axes since the orientation of the axes can be changed by transformation so that load paths can then be defined in arbitrary directions.

The vector field of “pointing vectors” for the required load path is first defined by averaging stresses to the nodes in the FE mesh. To plot the contours through the vector field a fourth order Runge-Kutta scheme can be used. The vector can be

(a) Construct for force component



(b) Contours for a path of constant P_x

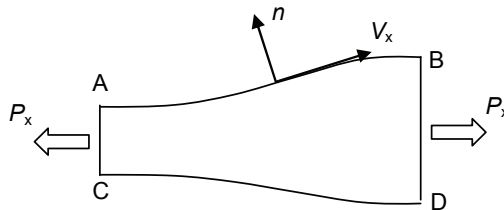


Figure 18: Construction of the paths

defined at any arbitrary point by first associating the point with an element and then interpolating from the nodes.

An example of the insight into functionality is the load transfer at a pin-loaded hole in Figure 19. Stress concentrations at the hole are identified from the convergence of the paths.

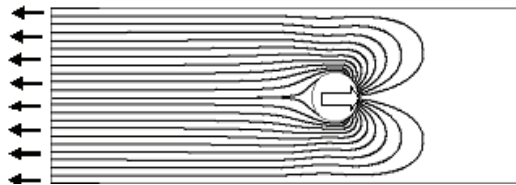


Figure 19: X-Force load path trajectories for a pin-loaded hole in an isotropic material

Figure 20 shows load paths of the D1 panel at 2.04 mm compression, which is taken from the FE analysis shown previously in Section 3. The colours correspond to the magnitude of these vectors and are not sign dependent. The stresses required

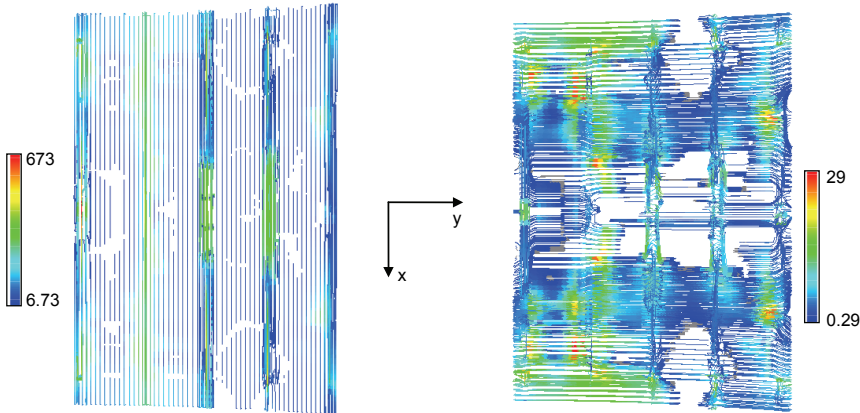


Figure 20: Load paths in the panel shown in Figure 8 at 2.04 mm compression. Left: X-direction. Right: Y-direction. Units are MPa

to plot the load paths are found by averaging the stresses in the plies that make up the laminates.

The left image shows the axial load in the panel plotted from the pointing vectors V_x . The paths are started from elements that are selected randomly and so there are more paths in the debonded stiffeners as the model has included separate elements for the skin and flange. The load is therefore identified by the colour of the plot and not the concentration of the paths. A cut-off is applied and the paths are not plotted if the magnitudes drop below 1% of the maximum value.

From this image, the second stiffener (counting from the left) carries the highest load and the load is shared by the surrounding skin. The skin between the other panels is more lightly loaded and appears to have been relieved by the buckles. The axial load increases in the third and fourth stiffeners as the stiffeners span the delaminations. This indicates that one mechanism driving crack growth is the shear at the ends of the delaminations that is required to equilibrate the load variation. Another interesting feature of the plot is the highly loaded (red) region developing in the stiffener on the left hand edge. This indicates plies in this blade could be the first to suffer fibre failure (recorded in the outer stiffeners at 2.25 mm end shortening in Section 3).

The second image maps the transverse loads in the panel plotted from V_y . The paths are initiated only from elements on the stiffener flanges and blades. The sides of the panel are not supported and so the transverse loads have to drop to zero at the sides. This plot provides some insight into the numerical algorithm. At this point in the load history the gap between the stiffener and the panel is open over the

debond. The light green paths over the debonds indicate the numerical algorithm allows some transfer of load in the transverse direction. As expected the transverse loads are small compared to the axial loads.

8 Discussion and Conclusion

The analyses presented for the panels demonstrate the capability to provide accurate predictions of the behaviour of postbuckling composite stiffened panels, and critically to capture the damage mechanisms for compression loading. The methodology has application for the design and analysis of the next generation of aircraft structures, as it allows for the significant efficiency gains from postbuckling design to be applied with composite materials.

One aspect that remains important in the application of the developed approach for both design and analysis is the computation time. For the analysis presented, computation times were dependent on the extent of crack growth and fibre fracture, and range from 40 minutes to more than a week on a single CPU for models where these factors were significant. It must be remembered that accurate analysis of crack growth and ply failure requires fine detail modelling and significant computational expense, and that experience is required to apply any damage model within a practical design and analysis procedure.

For all analyses conducted in the COCOMAT program, a number of factors considerably influenced comparison with experimental results. One aspect was the difficulty in accurately capturing the correct buckling mode shapes and deformation patterns, which is especially critical for crack growth in the region just ahead of any crack front. The work by the authors has identified the significant effect of manufacturing variability and uncertainty in the material properties. Wide variety was encountered in the experimental postbuckling shapes. The procedure developed here requires a survey of the variation encountered and implementation of FEA to a stochastically determined family of panels. The work indicated the mode shapes identified in the experiments could be recognised and categorised leaving no outliers in the data set available to the authors.

It can also be seen from the metamodels in Figure 11 that it is possible to reduce the deformation in the panels due to curing by controlling the quality of plies 1 and 2. This involves stringent quality control during the layup process and also the requirement that the material has less scatter.

Finally it is recognised that the aim of the COCOMAT program is to develop an understanding of the factors that influence the strength of imperfection sensitive compression panels. Preliminary results for a new initiative that attempts to map the load distribution in the panel have been described. It is expected that the work could

rank the importance of defects and artificially induced delaminations according to the participation of the structural members in the load paths up to collapse.

Acknowledgement: This research is part of the Research Program of the CRC-ACS. The authors kindly acknowledge the financial support of the following: the Australian Postgraduate Awards Scheme; the CRC-ACS; the German Academic Exchange Service; the Australian Government under both the “Innovation Access Programme – International Science and Technology” and “International Science Linkages” established under the Australian Government’s innovation statement, “Backing Australia’s Ability”. The work of the experimental testing staff at the Institute of Composite Structures and Adaptive Systems at DLR Braunschweig is also gratefully acknowledged. COCOMAT is supported by the European Commission, Priority Aeronautics and Space, Contract AST3-CT-2003-502723.

References

Benzeggagh, M.L., Kenane, M. (1996): Measurement of mixed-mode delamination fracture toughness of unidirectional glass/epoxy composites with mixed-mode bending apparatus. *Composites Science and Technology*, vol. 56, pp. 439–449.

Camanho, P.P., Dávila, C.G. (2003): Numerical simulation of mixed-mode progressive delamination in composite materials. *Journal of Composite Materials*, vol. 37, pp. 1415–1438.

Chang, F.K., Lessard, L.B. (1991): Damage tolerance of laminated composites containing an open hole and subject to compressive loadings: part I – analysis. *Journal of Composite Materials*, vol. 25, pp. 2–43.

Chryssanthopoulos, M.K., Poggi, C. (1995): Stochastic imperfection modeling in shell stiffened studies. *Thin-Walled Structures*, vol. 23, no. 15, pp. 179–200.

COCOMAT Home Page. (2009). www.cocomat.de

Degenhardt, R., Kling, A., Klein, H., Hillger, W., Goetting, H.C., Zimmermann, R., Rohwer, K., Gleiter, A. (2007): Experiments on buckling and post-buckling of thin-walled CFRP structures using advanced measurement systems. *International Journal of Structural Stability and Dynamics*, vol. 7, no. 2, pp. 337–358.

Degenhardt, R., Rolfes, R., Zimmerman, R., Rohwer, K. (2006): COCOMAT – Improved MATerial Exploitation at Safe Design of COmposite Airframe Structures by Accurate Simulation of COLLapse. *Composite Structures*, vol. 73, pp 178–178.

GOM GmbH. (2009): *Optical Measuring Techniques*. www.gom.com.

Hashin, Z. (1980): Failure criteria for unidirectional composites. *Journal of Ap-*

plied Mechanics, vol. 47, pp. 329–334.

Hexcel Corporation (2005): *Product data for HexPly 8552 epoxy resin*. www.hexcel.com.

Kelly, D.W., Hsu, P., Asadullah, M. (2001): Load paths and load flow in finite element analysis. *Engineering Computations*, vol. 18, pp. 304–313.

Krueger, R. (2004): Virtual crack closure technique: History, approach and applications. *Applied Mechanics Reviews*, vol. 57, no. 2, pp. 109–143.

Kulkarni, R., Ochoa, O. (2006): Transverse and longitudinal CTE measurements of carbon fibers and their impact on interfacial residual stresses in composites. *Journal of Composite Materials*, vol. 40, no. 8, pp. 733–754.

Lee, M., Kelly, D., Orifici, A.C., Thomson, R.S. (2007): Postbuckling mode shapes of stiffened composite fuselage panels incorporating stochastic variables. 1st CEAS European Air and Space Conference – Century Perspectives, Berlin, Germany, 10-13 September, 2007: 2977-2986.

Lee, M.C.W., Payne, R.M., Kelly, D.W., Thomson, R.S. (2008): Determination of robustness for a stiffened composite structure using stochastic analysis. *Composite Structures*, vol. 86, pp. 78–84.

Lee, M.C.W., Thomson, R.S., Degenhardt, R., Kelly, D.W. (2008): Imperfection investigation of composite stiffened fuselage panels for postbuckling analysis. *5th International Conference on Thin Walled Structures*, Brisbane, Australia, 18–20 June, 2008.

MSC Software Corporation. : *MSC.Nastran, and MSC.Patran (2008); MSC.Marc and MSC.Mentat User Manuals Version 2005r3*, Santa Ana, California, USA.

Orifici, A.C. (2007): *Degradation Models for the Collapse Analysis of Composite Aerospace Structures*. PhD thesis, Royal Melbourne Institute of Technology.

Orifici, A.C., Thomson, R.S., Degenhardt, R., Bayandor, J. (2008): The design of postbuckling composite aerospace structures accounting for damage initiation and growth. *26th Congress of International Council of the Aeronautical Sciences (ICAS 2008)*, Anchorage, USA, 14–19 September 2008.

Orifici, A.C., Thomson, R.S., Degenhardt, R., Bisagni, C., Bayandor, J. (2009a): A finite element methodology for analysing degradation and collapse in postbuckling composite aerospace structures. *Journal of Composite Materials*. (to appear).

Orifici, A.C., Thomson, R.S., Degenhardt, R., Bisagni, C., Bayandor, J. (2009b): An analysis tool for design and certification of postbuckling composite aerospace structures. *International Journal of Structural Stability and Dynamics*. (to appear).

Orifici, A.C., Thomson, R.S., Degenhardt, R., Bisagni, C., Bayandor, J. (2007): Development of a finite element methodology for the propagation of delaminations in composite structures. *Mechanics of Composite Materials*, vol. 43, no. 1, pp.

9–28.

Orifici, A.C., Thomson, R.S., Herszberg, I., Weller, T., Degenhardt, R., Bayandor, J. (2008): An analysis methodology for failure in postbuckling skin-stiffener interfaces. *Composite Structures*, vol. 86, pp. 186–193.

Raj, B.N., Iyengar, N.G.R., Yadav, D. (1998): Response of composite plates with random material properties using FEM and Monte Carlo Simulation. *Journal of Advanced Composite Materials*, vol. 7, no. 3, pp. 219–237.

Rybicki, E.F., Kanninen, M.F. (1977): A finite element calculation of stress intensity factors by a modified crack closure integral. *Engineering Fracture Mechanics*, vol. 9, pp. 931–938.

Spagnoli, A., Elghazouli, A.Y., Chryssanthopoulos, M.K. (2001): Numerical simulation of glass-reinforced plastic cylinders under axial compression. *Marine Structures*, vol. 14, no. 3, pp. 353–374.

Tong, T. (1997): An assessment of failure criteria to predict the strength of adhesively bonded double lap joints. *Journal of Reinforced Plastics and Composites*, vol. 16, pp. 698–715.